remote sensing

MDPI

Article

Weighted Mean Temperature Hybrid Models in China Based on Artificial Neural Network Methods

Meng Cai, Junyu Li *, Lilong Liu, Liangke Huang, Lv Zhou, Ling Huang and Hongchang He

College of Geomatics and Geoinformation, Guilin University of Technology, Guilin 541004, China
* Correspondence: junyu_li@whu.edu.cn; Tel.: +86-133-0783-5838

Abstract: The weighted mean temperature (T_m) is crucial for converting zenith wet delay to precipitable water vapor in global navigation satellite system meteorology. Mainstream T_m models have the shortcomings of poor universality and severe local accuracy loss, and they cannot reflect the nonlinear relationship between T_m and meteorological/spatiotemporal factors. Artificial neural network methods can effectively solve these problems. This study combines the advantages of the models that need in situ meteorological parameters and the empirical models to propose T_m hybrid models based on artificial neural network methods. The verification results showed that, compared with the Bevis, GPT3, and HGPT models, the root mean square errors (*RMSEs*) of the new three hybrid models were reduced by 35.3%/32.0%/31.6%, 40.8%/37.8%/37.4%, and 39.5%/36.4%/36.0%, respectively. The consistency of the new three hybrid models was more stable than the Bevis, GPT3, and HGPT models in terms of space and time. In addition, the three models occupy 99.6% less computer storage space than the GPT3 model, and the number of parameters was reduced by 99.2%. To better evaluate the improvement of hybrid models T_m in the precipitable water vapor (PWV) retrieval, the PWVs calculated using the radiosonde T_m and zenith wet delay (ZWD) were used as the reference. The *RMSE* of PWV derived from the best hybrid model's T_m and the radiosonde ZWD meets the demand for meteorological research and is improved by 33.9%, 36.4%, and 37.0% compared with that of Bevis, GPT3, and HGPT models, respectively. The hypothesis testing results further verified that these improvements are significant. Therefore, these new models can be used for high-precision T_m estimation in China, especially in Global Navigation Satellite System (GNSS) receivers without ample storage space.

Keywords: weighted mean temperature; global navigation satellite system meteorology; artificial neural network; empirical model; hybrid model

Citation: Cai, M.; Li, J.; Liu, L.; Huang, L.; Zhou, L.; Huang, L.; He, H. Weighted Mean Temperature Hybrid Models in China Based on Artificial Neural Network Methods. *Remote Sens.* **2022**, *14*, 3762. https://doi.org/10.3390/rs14153762

Academic Editors: Xiaoming Wang, Suelynn Choy, Kefei Zhang, Karina Wilgan and Haobo Li

Received: 19 May 2022
Accepted: 3 August 2022
Published: 5 August 2022

1. Introduction

Water vapor is an essential component of the Earth's atmosphere and is crucial for global atmospheric radiation, water cycle, and energy balance [1,2]. Study on water vapor's spatial and temporal distribution is quite important in weather and climate forecasting. The GNSS signals propagating through the troposphere are delayed and bent due to the nonvacuum conditions, known as tropospheric delays [3–5]. The tropospheric delay is the zenith total delay (ZTD) multiplied by the tropospheric mapping function, and ZTD consists of zenith hydrostatic delay and zenith wet delay. The GNSS zenith wet delay can be converted into precipitable water vapor using Weighted Mean Temperature (T_m) [6]. Therefore, obtaining a high-precision T_m is crucial for improving the accuracy of GNSS retrieving precipitable water vapor [6–12]. Previous studies have shown that GNSS-derived PWV is accurate and reliable, with *RMSE* of 1–3 mm [6,13].

An accurate way to obtain high-precision T_m is to integrate the vertical profiles of temperature and humidity. However, these profiles are often challenging to obtain in practical work, and thus currently the T_m models are usually used to calculate the T_m. These models can be divided into two categories. The first category is the model that needs in situ

meteorological parameters. Bevis et al. [6] analyzed the correlation between the surface temperature (T_s) and T_m of radiosonde data in North America. They found an excellent linear correlation between T_m and T_s, thereby proposing a linear regression formula of T_m ($T_m = a + bT_s$). Since the model coefficients have significant seasonal and local characteristics, to obtain high-precision T_m values in other regions, the coefficients of the Bevis formula need to be re-estimated from local radiosonde data [14,15]. Therefore, many scholars have established regional models for different areas [16–18]. These models have high accuracy; however, they are only applicable to certain areas and cannot reflect the delicate nonlinear relationship between T_m and meteorological factors. Another model [19,20] is an empirical model driven by spatiotemporal information, which does without in situ meteorological parameters and can generate empirical T_m for large area or even global locations. Leandro et al. [21] used relative humidity to replace the water vapor pressure in the parameter table of the UNB3 model and established the UNB3m model. The UNB3m model considers the annual cyclic variation of meteorological parameters, has a resolution of 15 latitudes, and can be used to calculate T_m. Yao et al. [22] used the GGOS grid T_m with a 6 h resolution to analyze the daily variation characteristics of T_m, and they constructed a new global T_m model (GTm-III) that considers the diurnal variation of T_m. Subsequently, Böhm et al. [19] established the GPT2w model, which can provide vital tropospheric parameters such as T_m and water vapor pressure with a horizontal resolution of up to $1^\circ \times 1^\circ$. Landskron et al. [23] proposed the GPT3 model, which incorporated meteorological parameter data directly from the GPT2w model; hence, T_m in the GPT3 model is consistent with GPT2w. Sun et al. [24] used ERA5 data to establish a new model integrating tropospheric delay correction for GNSS positioning and T_m calculation for GNSS meteorology. The model has a spatial resolution of $0.5^\circ \times 0.5^\circ$ and a temporal resolution of 1 h. Mateus et al. [25] developed an hourly global pressure and temperature (HGPT) model based on the full spatial and temporal resolution of the new ERA5 reanalysis. The HGPT model can provide hourly surface pressure, surface air temperature, zenith hydrostatic delay, and weighted average temperature information with a spatial resolution of $0.25^\circ \times 0.25^\circ$. As the spatiotemporal factors considered by the empirical model increase, the models' overall accuracy gradually improves, but it also increases the number of model parameters. In addition, scholars have also developed many similar empirical models [20,26,27]. Although these empirical models are driven by spatiotemporal information and convenient for use and have strong universality, their accuracy is inferior to the model that needs in situ meteorological parameters mentioned above, especially in areas with relatively sparse weather stations and large terrain fluctuations. Still, it is difficult to reflect the delicate nonlinear relationship between T_m and spatiotemporal factors; therefore, the accuracy of the T_m model needs to be further improved. Artificial neural network methods have been widely used in various industries due to their nonlinear fitting ability [28–31].

In this study, we hope to establish several T_m models with higher accuracy than the approved T_m models, such as Bevis, GPT3, and HGPT, through artificial neural networks, and these models require fewer parameters. Consequently, the PWV converted by the T_m from the new models can meet the requirements of meteorological research. To achieve this goal, we used artificial neural network methods to fit the relationship between high-precision radiosonde T_m, empirical T_m (provided by the UNB3m model with few parameters), meteorological parameters, and spatiotemporal factors, and then built high-precision T_m models.

2. Study Area and Methods for Calculating T_m

2.1. Study Area

The research area spans 70°E–135°E and 15°N–55°N, which covers the land of China and some surrounding countries and regions (see Figure 1). In this study, we accessed radiosonde data from the Integrated Global Radiosonde Archive (IGRA). Data from 150 radiosonde stations in the study area were obtained for the experiments. The distribution of the stations is indicated by the red triangles in Figure 1.

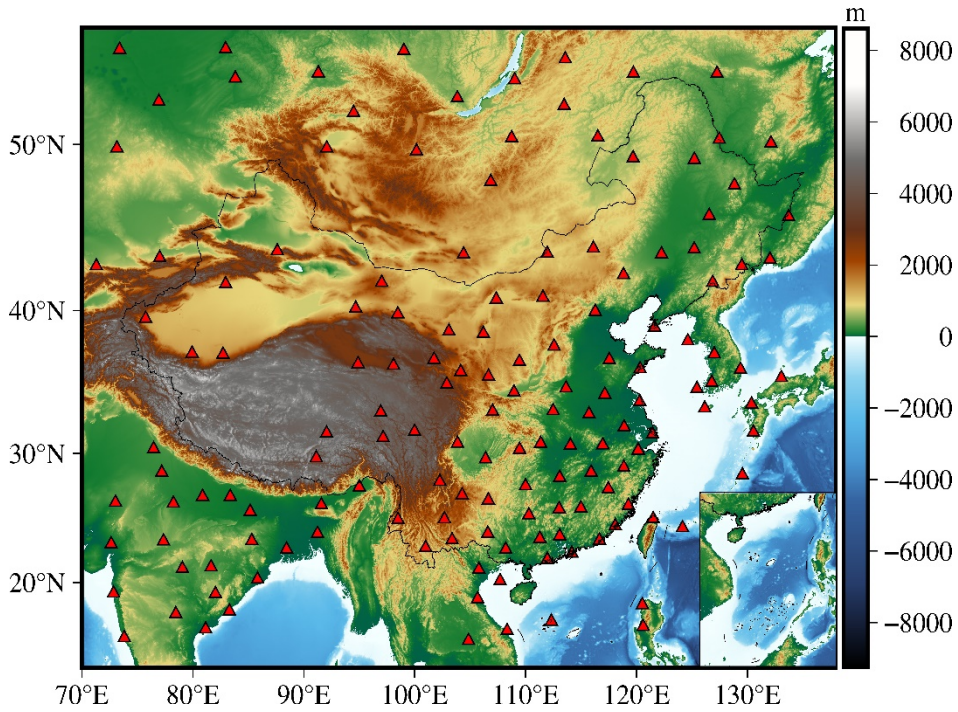

Figure 1. Study terrain and distribution of radiosonde stations (marked with red triangles).

2.2. Method of Calculating T_m

2.2.1. Calculation of T_m Based on Radiosonde Data

Radiosonde data are important meteorological observation data. The IGRA has provided high-quality sounding observations from more than 1500 radiosondes and sounding balloons worldwide since the 1960s and launches radiosonde twice daily at 00:00 and 12:00 UTC. This study used data from 150 radiosonde stations (2007–2016) to calculate T_m according to the following formula [6]. It is worth mentioning that during long-term continuous observations, the radiosonde data may have discontinuities and outliers. Since these values will affect the results of the new model establishment, this study used the interquartile range (IQR) method to remove outliers in the long-term series of radiosonde data [32].

$$T_m = \frac{\int (e/T) dH}{\int (e/T^2) dH} \tag{1}$$

where T is the absolute temperature (K). e is the water vapor pressure (hPa), which is calculated from the relative humidity (RH) using Equations (2) and (3) [6,10]:

$$e_s = 6.11 \times 10^{\left(\frac{7.5 \times T_d}{237.3 + T_d}\right)} \tag{2}$$

$$e = RH \cdot e_s / 100 \tag{3}$$

where e_s is the saturated vapor pressure (hPa) and T_d is the dew point temperature (°C).

2.2.2. Calculating T_m Based on the UNB3m Model

The UNB3m model is based on a look-up table with annual mean and amplitude for temperature, pressure, temperature lapse rate, and water vapor pressure height factor. These parameters are calculated for a particular latitude and day of year using a cosine

function for the annual variation and a linear interpolation for latitude. The annual average value of the meteorological parameters is calculated using the following formula:

$$AVG_\varphi = \begin{cases} AVG_{15}, \varphi \le 15^\circ \\ AVG_{75}, \varphi \ge 75^\circ \\ AVG_i + \frac{(AVG_{i+1} - AVG_i)}{15}(\varphi - LAT_i), 15^\circ < \varphi < 75^\circ \end{cases} \quad (4)$$

where φ is the latitude of the target point (°), AVG_φ is the annual mean value, i is the latitude band closest to the target location that has a smaller value, and LAT_i is the value of the corresponding latitude band. The formula for calculating the annual cycle amplitude is as follows:

$$AMP_\varphi = \begin{cases} AMP_{15}, \varphi \le 15^\circ \\ AMP_{75}, \varphi \ge 75^\circ \\ AMP_i + \frac{(AMP_{i+1} - AMP_i)}{15}(\varphi - LAT_i), 15^\circ < \varphi < 75^\circ \end{cases} \quad (5)$$

where AMP_φ denotes the annual cycle amplitude. The meteorological parameter values at a specified time at the target point can be calculated by entering the mean yearly value and annual periodic amplitude value of the target parameter into the trigonometric function:

$$X_{\varphi,doy} = AVG_\varphi - AMP_\varphi cos\left((doy - doy_0)\frac{2\pi}{365.25}\right) \quad (6)$$

where $X_{\varphi,doy}$ is the annual periodic amplitude value, doy is the day of the year, and doy_0 specifies the initial phase of the regular change, which is 28 in the Northern Hemisphere and 211 in the Southern Hemisphere.

The UNB3m model can calculate T_m according to the following formula:

$$T_m = (T_0 - \beta H)\left(1 - \frac{\beta R}{g_m(\lambda + 1)}\right) \quad (7)$$

where T_0, β, and λ are the meteorological parameters calculated according to procedures (4)–(6), which are temperature (K), temperature lapse rate (K/m), and water vapor pressure height factor, respectively; H is the orthometric height (m); R is the gas constant for dry air (287.054 J/kg/K); and g_m is the acceleration of gravity at the atmospheric column centroid (m/s^2), which can be expressed as

$$g_m = 9.784\left(1 - 2.66 \times 10^{-3} cos(2\varphi) - 2.8 \times 10^{-7} H\right) \quad (8)$$

The above model has few parameters and is convenient and straightforward to use; however, the UNB3m model only considers the variation of T_m with latitude, and his grid is too sparse, so the accuracy is limited [33].

2.2.3. Calculating T_m Based on the GPT3 Model

The global pressure and temperature 3 (GPT3) model proposed by Landskron and Bohm is the latest version of the GPT series [23]. The meteorological parameters of the GPT3 model are the same as that of GPT2w with admirable performance. It is one of the most widely used models [10,31]. GPT3 characterizes T_m seasonal variations based on the following Equation (9) and takes into account their geographical variations by 1° × 1° or 5° × 5° grids.

$$r(t) = A_0 + A_1 cos\left(\frac{2\pi t}{365.25}\right) + B_1 sin\frac{2\pi t}{365.25} + A_2 cos\frac{4\pi t}{365.25} + B_2 sin\frac{4\pi t}{365.25} \quad (9)$$

where *r(t)* is the meteorological parameters to be estimated; t denotes the day of year; A_0 represents its mean value; and (A_1, B_1) and (A_2, B_2) are their annual and semiannual amplitudes, respectively.

3. Construction of Hybrid Model

In this study, we use Backpropagation neural network (BPNN), Random Forest (RF), and Generalized Regression Neural Network (GRNN) in the neural network toolbox of MATLAB software to optimize UNB3m T_m by using high-precision radiosonde T_m data, then construct three hybrid models.

3.1. Three Artificial Neural Network Methods

3.1.1. BPNN

The BPNN, first proposed by Rumelhart et al. [34], is one of the most widely used ANNs. The network adopts the gradient descent method to minimize the differences between the network output and target output [35].

The BPNN consists of an input layer, a hidden layer, and an output layer. The number of neurons in the input layer of the BPNN is equal to the number of input variables, and the number of neurons in the output layer is equal to the number of output variables. Almost every bounded continuous function can be approximated with an arbitrarily minor error using a neural network with a single hidden layer [36]. Therefore, in this study, we chose the number of hidden layers as a single layer and determined the number of neurons in the hidden layer in Section 3.3.

Because the empirical model optimized in this study is the UNB3m model, UNB3m T_m must be used as an essential input for the artificial neural network model. UNB3m T_m is established considering the variations in the latitude, height, and day of year, so there must be a strong correlation between UNB3m T_m and latitude, height, and day of year. Simultaneously, some studies [4,19,24] found that there exist long-term interannual variations and diurnal variations in T_m, so we take year, hour of day (hod), latitude (lat), height, and day of year (doy) as input variables.

It is well known that the surface temperature (T_s) and water vapor pressure (e_s) have strong relationships with the observation T_m [6,11], and the T_m models based on in situ T_s/e_s observations can reach higher precision than empirical models. Thus, the T_s/e_s were employed as inputs for the new model. Li et al. [5] suggested that UNB3m often causes great prediction tropospheric delay biases in some areas because it is only based on latitude–label meteorological parameters that are also needed for calculating T_m. Moreover, many T_m models [11,19,25], considering the longitude variations, have excellent performance. Therefore, we also took longitude as an input variable. It should be noted that the widespread distribution of surface meteorological observation facilities, T_s and e_s, can be obtained in real-time in most regions [37]. Therefore, it is not difficult to obtain the temperature and water vapor pressure to support the operation of the new model, and establishing the T_m model based on meteorological parameters has a good potential for real-time application. Table 1 shows all the input parameters and the output parameter. In addition, when training the model, the radiosonde-derived T_m was loaded into the output layer, and the output layer outputs the corrected T_m value when used. The structure of the BPNN T_m model is shown in Figure 2.

Table 1. Main features of the hybrid models.

Input parameters	surface temperature (T_s), water vapor pressure (e_s), year, day of year (doy), and hour of day (hod), latitude, longitude, height, and UNB3m-T_m
Output parameter	T_m

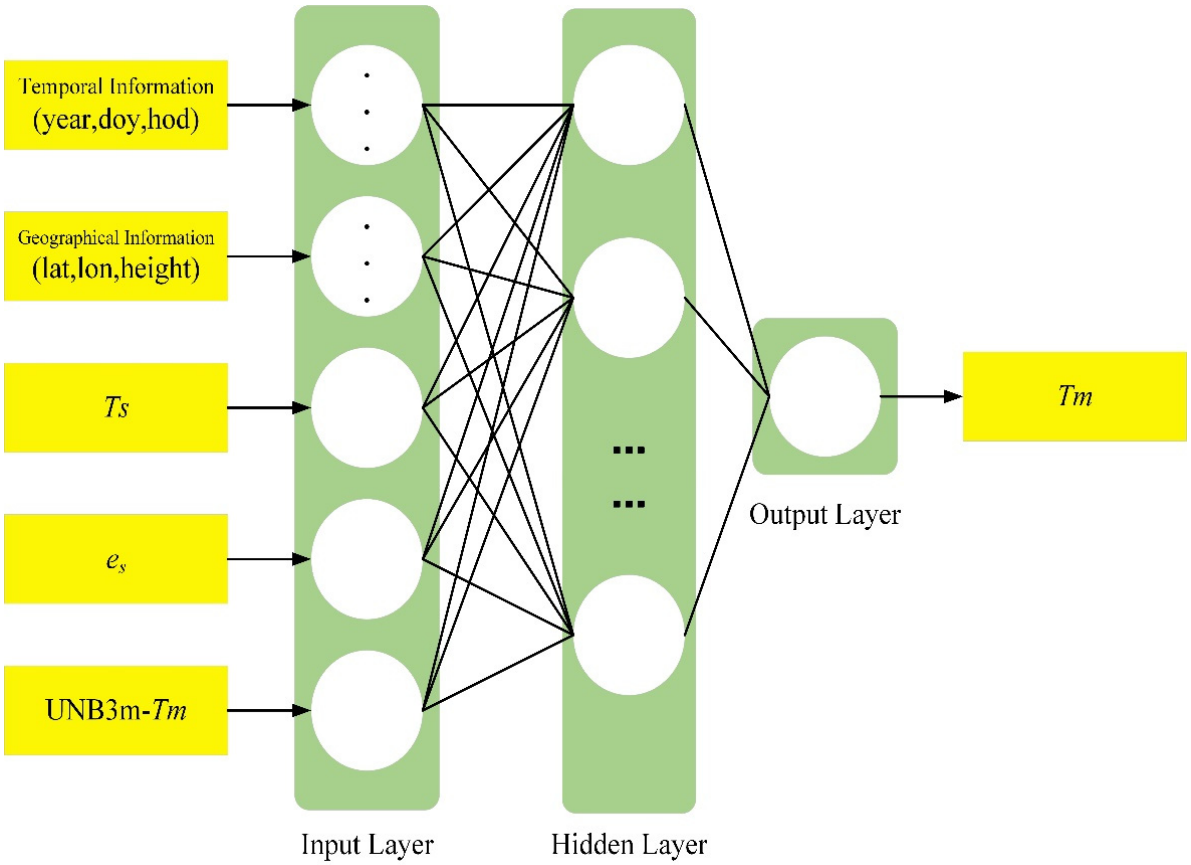

Figure 2. Structural diagram of backpropagation neural network.

The process of training the BPNN includes forward and backpropagation. Each neuron in each layer of the BPNN model is directly connected to the neurons in the next layer and had an activation function. This study used the hyperbolic tangent function to activate the input and hidden layer neurons. A linear function was used to activate the neurons of the hidden and output layers. The equations are represented as:

$$g(x) = \frac{2}{1 + \exp(-2x)} - 1 \tag{10}$$

$$f(x) = x \tag{11}$$

Then the final output of BPNN can be expressed as:

$$Y(X) = f(W_{3,2} \cdot g(W_{2,1} \cdot X + b_1) + b_2) \tag{12}$$

where $W_{2,1}$ and $W_{3,2}$ represent the weight matrix, b_1 and b_2 represent the bias matrix. These four matrices store the coefficients of the BPNN model. X and Y are the input and output variables, respectively.

3.1.2. RF

Breiman and Cutler first proposed a random forest in 2001 [38]. RF is an ensemble learning method used for classification and regression. RF works by constructing many decision trees during training and then outputting the mode of the classes or the average prediction of the individual trees [38]. RF has the advantages of fast training speed and handling complex nonlinear relationships between the input and output variables. The structure of the RF T_m model is shown in Figure 3. The input data included time (year, day of year, and hour of day), location (latitude, longitude, and height), e_s, T_s, and UNB3m-T_m.

In addition, the output data were radiosonde-derived T_m or the corrected T_m. Because overfitting can occur with a single decision tree, RF overcomes this problem by introducing randomness into each decision tree and averaging the results. The result of the model was the mean of the consequences of all constructed decisions, as shown in the following formula:

$$Y(X) = \frac{1}{B}\sum_{b=1}^{B} T_b(X) \tag{13}$$

where X represents the input variable, Y is the final RF output value, T_b denotes the output value of each decision tree, and B represents the number of decision trees. The number of decision trees directly affected the accuracy of the RF model. Because the number of decision trees must be optimally selected, the enumeration method is generally used. The specific number value is determined in Section 3.3.

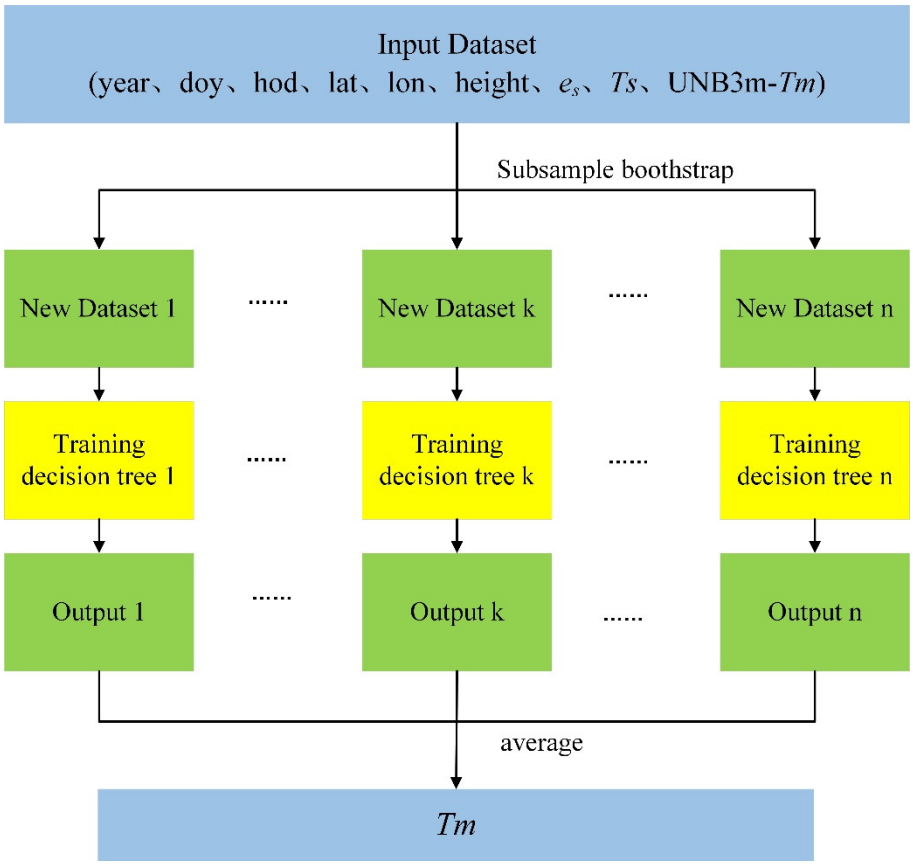

Figure 3. Structural diagram of random forest.

3.1.3. GRNN

Specht first proposed GRNN in 1991 [39]. The GRNN neural network is a radial basis function network based on mathematical statistics. The GRNN has a strong nonlinear mapping ability and learning speed, and the network can also handle unstable data. The GRNN consists of four layers: the input, pattern, summation, and output layers. The number of neurons in the input layer corresponds to the number of input variables; nine neurons correspond to the time information (year, day of year, and hour of day), location information (latitude, longitude, and height), e_s, T_s and UNB3m-T_m. The number of neurons in the output layer corresponds to the number of output variables. In this experiment, the output layer had only one neuron corresponding to the radiosonde T_m or the model-corrected T_m. The summation layer includes two types of summation neurons, which perform arithmetic summation and weighted summation of the output values of the

pattern layer. The number of neurons in the pattern layer corresponds to the number of training samples, and the transmission of neurons can be expressed as:

$$p_i = exp\left\{-\frac{(X - X_i)^T(X - X_i)}{2\sigma^2}\right\}, i = 1, 2, \ldots, n \quad (14)$$

where p_i is the output of the i neuron in the pattern layer, represented by the exponential function of the square of the Euclidean distance between the input variable X_i (the i-th learning sample) and its corresponding test sample. σ represents the spread parameter, the only unknown parameter in the network, and needs to be set first. It is necessary to determine the optimal spread parameter as a σ, which, when too large, may make the estimation very smooth or, when too small, may result in a value too close to the sample value [39]. The specific value is defined in Section 3.3. The structure of the GRNN T_m model is shown in Figure 4.

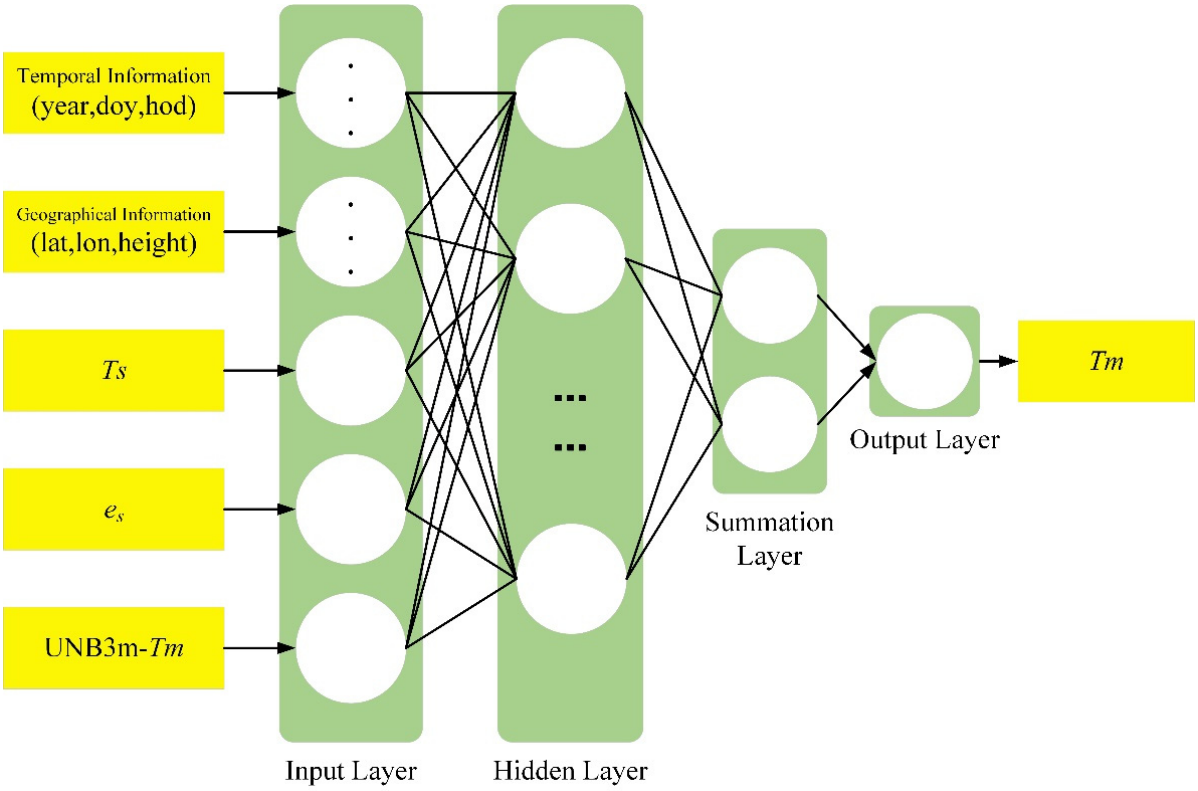

Figure 4. Structural diagram of generalized regression neural network.

3.2. Evaluation Indicators Adopted by the Model

This experiment adopted a 10-fold cross-validation method to evaluate the different artificial neural network models [40]. The basic principle of the 10-fold cross-validation technique is to randomly split the dataset into 10 groups and then select 9 groups as the training set and 1 group as the test set. This process was repeated 10 times, so each part of the dataset was tested once, trained 9 times, and all residuals were computed and saved. Note that it can ensure that more data is involved in the training so that the results are closer to the accuracy of the final model and can also prevent overfitting. We calculated five statistical indicators based on these residuals to evaluate model performance. These indicators are the *bias*, mean absolute error (*MAE*), standard deviation (*STD*), root

mean square error (*RMSE*), and Pearson correlation coefficient (*R*). The formulas of these indicators are as follows:

$$Bias = \frac{1}{N}\sum_{i=1}^{N}\left(T_{k,i}^{hm} - T_{k,i}^{rs}\right) \tag{15}$$

$$MAE = \frac{1}{N}\sum_{i=1}^{N}\left|T_{k,i}^{hm} - T_{k,i}^{rs}\right| \tag{16}$$

$$STD = \sqrt{\frac{1}{N}\sum_{i=1}^{N}\left(T_{k,i}^{hm} - T_{k,i}^{rs} - Bias\right)^2} \tag{17}$$

$$RMSE = \sqrt{\frac{1}{N}\sum_{i=1}^{N}\left(T_{k,i}^{hm} - T_{k,i}^{rs}\right)^2} \tag{18}$$

$$R = \frac{\sum_{i=1}^{N}\left(T_{k,i}^{hm} - \overline{T_{k,i}^{hm}}\right)\left(T_{k,i}^{rs} - \overline{T_{k,i}^{rs}}\right)}{\sqrt{\sum_{i=1}^{N}\left(T_{k,i}^{hm} - \overline{T_{k,i}^{hm}}\right)^2 \sum_{i=1}^{N}\left(T_{k,i}^{rs} - \overline{T_{k,i}^{rs}}\right)^2}} \tag{19}$$

where N is the number of samples, $T_{k,i}^{hm}$ is the T_m value output by the hybrid models, $T_{k,i}^{rs}$ is the T_m values derived from the radiosonde data, and $\overline{T_{k,i}^{hm}}$, $\overline{T_{k,i}^{rs}}$ are the mean values of $T_{k,i}^{hm}$ and $T_{k,i}^{rs}$, respectively.

After verifying the accuracy and reliability of the hybrid models using 10-fold cross-validation, we fitted all samples to generate the final model for subsequent T_m prediction. When users want to use the hybrid models to calculate T_m, they only need to collect T_s and e_s and then input them with the time and location information into the models' code.

3.3. Parameter Determination

In this experiment, the number of neurons in the BPNN hidden layer, the number of RF decision trees, and the GRNN spread value are the parameters that need to be set first. We followed Sun et al. [41] to set up the crucial parameters. For the BPNN, the optimal number of neurons in the hidden layer can be selected in the range of $2\sqrt{n} + \mu$ to $2n + 1$ (n is the number of neurons in the input layer, μ is the number of neurons in the output layer) [42,43]; therefore, the experiment used a 10-fold cross-validation technique to test the BPNN models with 7 to 19 hidden layer neurons. For RF, we set the number of decision trees between 5 and 95 with a step size of 10 and then used 10-fold cross-validation to test the performance of RF models with different numbers of decision trees. For GRNN, the spread value used is usually in the range of 0.01 to 1 [28]. After many tests, we found that the optimal spread value was between 0 and 0.1; therefore, this experiment narrowed the selection range from 0.01 to 0.1, with a step size of 0.01. Similarly, we used a 10-fold cross-validation technique to test the performance of GRNN models with different spread values. Finally, the root mean square errors (*RMSE*) calculated from the cross-validation residuals were used to evaluate the performance of the other models with different parameter settings. The results are shown in Figure 5.

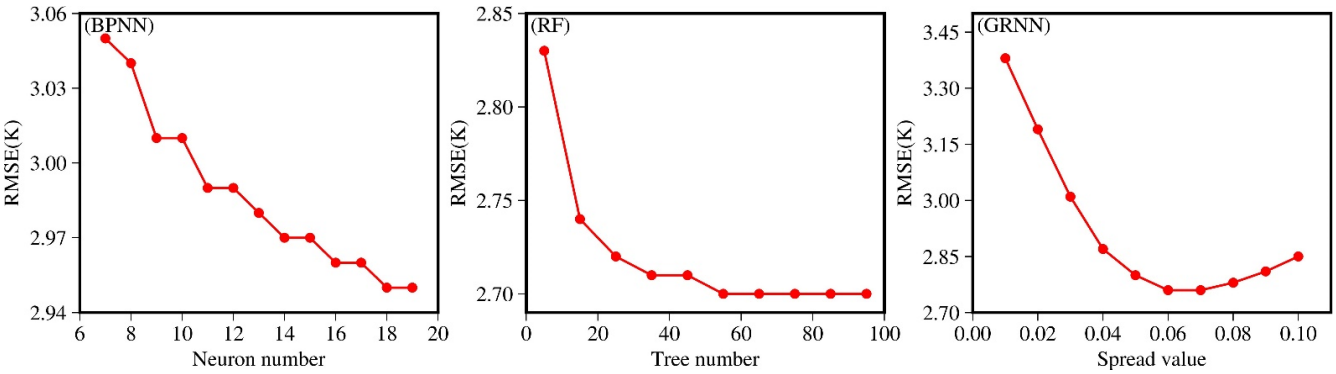

Figure 5. Statistical diagram of *RMSE* of different models with different parameter settings based on a 10-fold cross-validation technique.

In the BPNN model, the *RMSE* gradually decreased as the number of neurons in the hidden layer increased. This decline stopped when the number of neurons reaches 18. Therefore, we can set 18 or 19 as the number of hidden layer neurons. When the neuron number changed from 18 to 19, we found that the *RMSE* was equal, but a very long training time was required. Therefore, we set the number of neurons in the hidden layer to 18. In the RF model, when the number of decision trees increased from 5 to 55, the *RMSE* decreased significantly. But this decrease closed out after the number of decision trees exceeded 55. Thus, we set the number of decision trees to 55 to reduce the complexity of the model. In the GRNN model, when the spread value increased from 0 to 0.06, the *RMSE* gradually decreased; however, after the spread value exceeded 0.06, the *RMSE* gradually increased. Therefore, we finally chose 0.06 as the spread value.

4. Performance Analyses of Hybrid Models

In this study, the three hybrid models constructed using the three artificial neural network methods of BPNN, RF, and GRNN are named hybrid model 1, hybrid model 2, and hybrid model 3 (referred to as hm1, hm2, and hm3, respectively). The Bevis model ($T_m = 70.2 + 0.72T_s$) needs in situ meteorological parameters as input and is commonly used internationally. The GPT3 model is an empirical model that is widely used, and it is a grid model that also can reflect the characteristics of T_m in a certain area. Its accuracy performance in China can be used to represent mainstream empirical models. The HGPT model [25] is a recently released T_m model with open source code. Therefore, the Bevis, GPT3 ($1^\circ \times 1^\circ$), and HGPT models were chosen to compare with the new models.

4.1. Overall Performance

After determining the parameters of the three artificial neural network methods, the experiment selected 936,034 samples from 2007 to 2016 for training and obtained the corresponding models and results. The cross-validation and model fitting accuracy results are listed in Table 2. Note that since the 10-fold validation uses all the data to verify the model's accuracy, the validation results here span from 2007 to 2016. Scatter plots between the T_m values obtained from different models and the T_m values derived from the radiosonde data are shown in Figures 6 and 7. In Figures 6 and 7, the color indicates data density.

Table 2. Relative radiosonde data, the accuracy evaluation results of different models.

Model		Hyperparameter	*Bias* (K)	*MAE* (K)	*STD* (K)	*RMSE* (K)	*R*
UNB3m	-	-	−1.97	8.41	10.78	10.955	0.540
Hm1	Cross-V	18	0.00	2.28	2.95	2.954	0.969
	Fitting	18	0.00	2.28	2.95	2.953	0.969
Hm2	Cross-V	55	0.00	2.07	2.70	2.703	0.974
	Fitting	55	0.00	1.62	2.10	2.096	0.984
Hm3	Cross-V	0.06	0.02	2.09	2.76	2.763	0.973
	Fitting	0.06	0.01	1.59	2.10	2.101	0.984
Bevis	-	-	0.80	3.53	4.49	4.563	0.931
GPT3	-	-	−0.48	3.35	4.31	4.340	0.932
HGPT	-	-	0.00	3.33	4.32	4.317	0.932

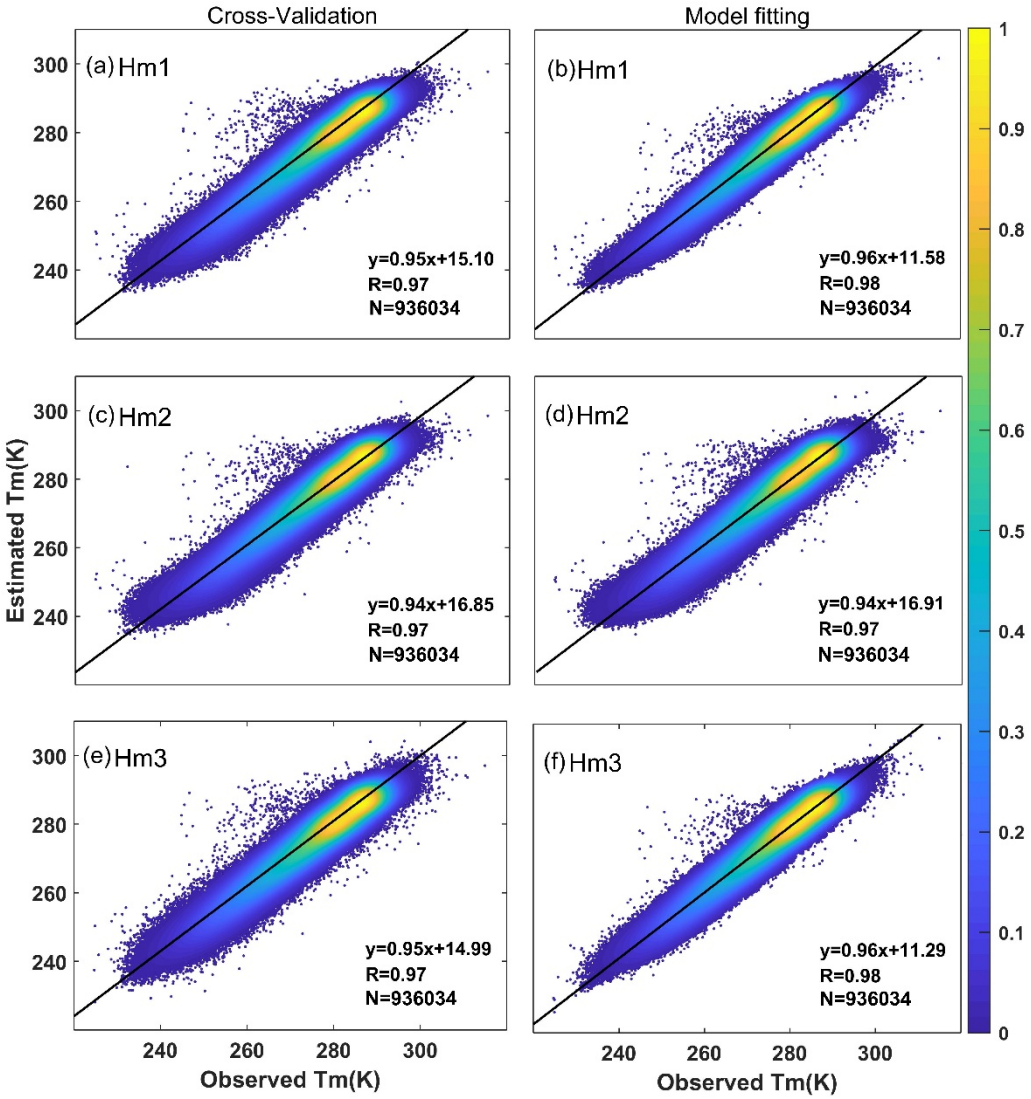

Figure 6. Scatter plots of estimated T_m against T_m derived from radiosonde data for different models: (**a**) hybrid model 1 cross-validation; (**b**) hybrid model 1 fitting; (**c**) hybrid model 2 cross-validation; (**d**) hybrid model 2 cross-validation; (**e**) hybrid model 3 cross-validation; (**f**) hybrid model 3 fitting.

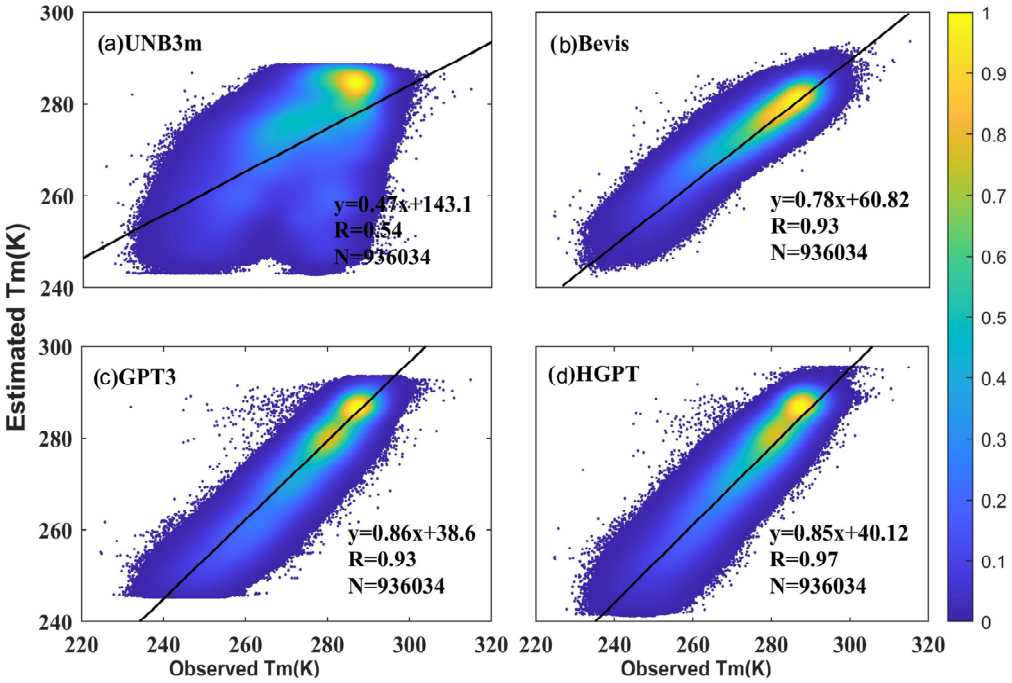

Figure 7. Scatter plots of estimated T_m against T_m derived from radiosonde data for different models: (**a**) UNB3m model; (**b**) Bevis model; (**c**) GPT3 model; (**d**) HGPT model. (The cut in the GPT3 (**c**) is due to there being no data in that range.).

Table 2 shows that the *biases* of the UNB3m model, the Bevis model, and the GPT3 model are −1.97 K, 0.80 K, and −0.48 K, respectively. The results indicate that there are systematic *biases* in the three models. However, the *biases* of the three hybrid models are all close to zero, which suggests that the artificial neural network method successfully corrects systematic *biases*. Because the artificial neural network methods successfully removed systematic *biases*, the *STDs* and *RMSEs* were nearly equal. After being corrected by the three hybrid models, the *RMSEs* are reduced to 2.954 K, 2.703 K, and 2.763 K, which are 73.1%, 75.3%, and 74.8% lower than the UNB3m model, respectively. By using the analysis of variance (ANOVA), it is further demonstrated that the T_m of the three hybrid models is not significantly different from the radiosonde T_m ($p > 0.05$). Meanwhile, relative to the Bevis model, the *RMSEs* were reduced by 35.3%, 40.8%, and 39.5%; for the GPT3 model, the *RMSEs* were reduced by 32.0%, 37.8%, and 36.4%; for the HGPT model, the *RMSEs* were reduced by 31.6%, 37.4%, and 36.0% respectively. After improving the three artificial neural network methods, the correlation coefficient R increased from 0.540 to 0.969, 0.974, and 0.973. The above analysis shows that all three artificial neural network methods significantly improved the accuracy of the UNB3m model in calculating T_m. These improvements may be accounted for by the strong ability of artificial neural network methods to fit complex nonlinear relationships. (The discussion will be described in the following paragraph.) In addition, when comparing the three hybrid models, we can see that the accuracy validation result of hm2 is smaller than those of hm1 and hm3. Therefore, hm2 exhibited a more stable performance.

To illustrate whether the improvement in accuracy of the three hybrid models comes from the data source or the method, we developed a linear model named LS model, which has the same input parameters as the three hybrid models using the least-squares method. The LS model is based on the same modeling data set as the hybrid model, and the specific formula is as follows:

$$T_m = a_1 + a_2 \cdot T_s + a_3 \cdot e_s^{a_4} + a_5 \cdot h + a_6 \cdot lon + a_7 \cdot lat + a_8 \cdot cos\left(\frac{DOY - a_9}{365.25} 2\pi\right) + a_{10} \cdot cos\left(\frac{DOY - a_{11}}{365.25} 4\pi\right) + a_{12} \cdot cos\left(\frac{HOD - a_{13}}{24} 2\pi\right) + a_{14} \cdot cos\left(\frac{HOD - a_{15}}{24} 4\pi\right) \quad (20)$$

Then, the accuracy of the hybrid models, LS model, Bevis model, GPT3 model, and HGPT model are compared. The results are shown in Table 3.

Table 3. The overall accuracy of different models.

Model	*RMSE* (K)
Hm1	2.954
Hm2	2.703
Hm3	2.763
LS model	3.340
Bevis	4.563
GPT3	4.340
HGPT	4.317

Table 3 shows that the *RMSE* of the LS model has been improved to different degrees when compared with that of the Bevis, GPT3, and HGPT models, which should be due to the use of the T_s, e_s, and T_m data in the study area to fit the relationship between them. Using the same data source, the *RMSE* of the three hybrid models increased by 13.2%, 23.7%, and 21.0% compared with the LS model. This improvement should be due to the method that can fit the nonlinear relationship between different parameters.

4.2. Spatiotemporal Performance of the Hybrid Models

In this section, we calculate the *RMSEs* of 150 radiosonde stations to analyze the spatial performance of the hybrid models. Figure 8 shows the specific values and distributions. Figure 9 shows the frequencies of the *RMSEs* for each interval. The numbers over the bars represent the number of stations within the corresponding *RMSE* range. Figures 8 and 9 also include the *RMSEs* of the UNB3m, Bevis, GPT3, and HGPT models at each radiosonde station.

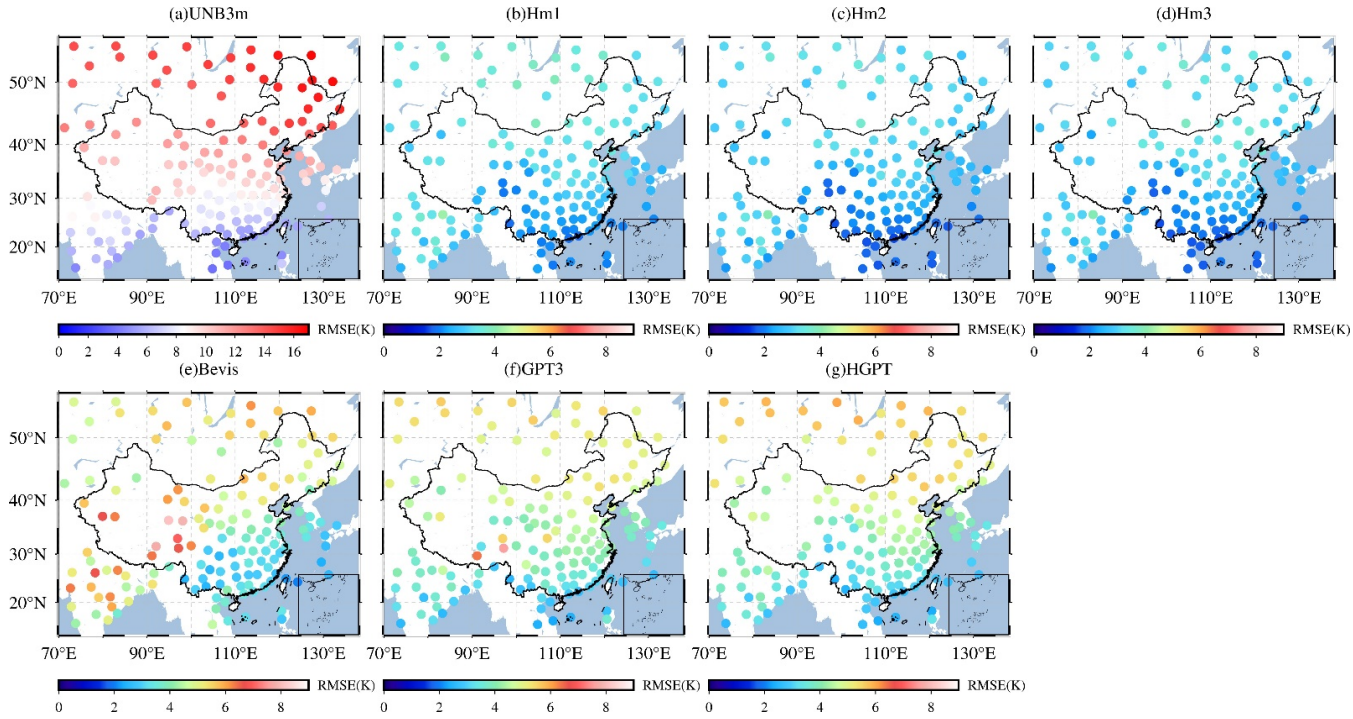

Figure 8. Spatial distribution of the *RMSE* that are calculated cross-validation residuals at each radiosonde station for (**a**) UNB3m model, (**b**) Hybrid model 1, (**c**) Hybrid model 2, (**d**) Hybrid model 3, (**e**) Bevis model, (**f**) GPT3 model, and (**g**) HGPT model.

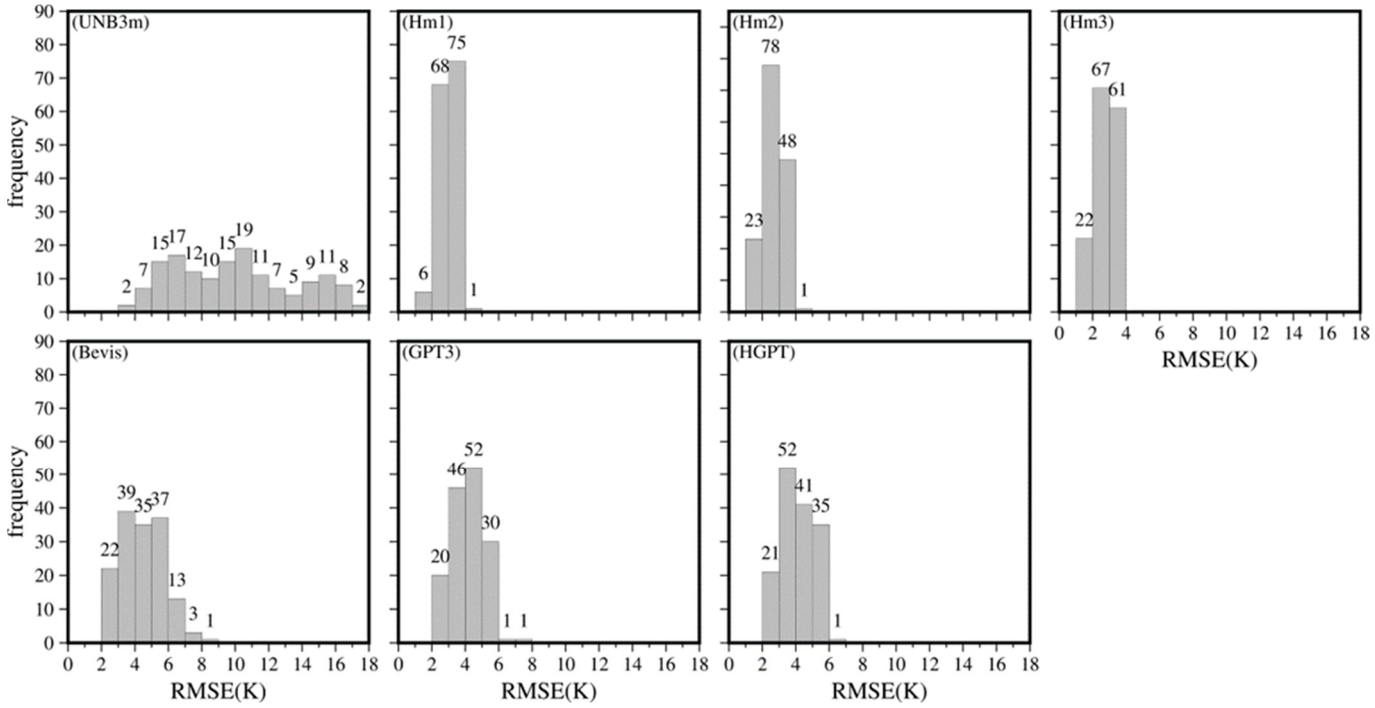

Figure 9. Statistics of *RMSEs* at each radiosonde station of each model.

As shown in Figure 8, regardless of the model used, low latitudes show a smaller *RMSE* and high latitudes show a larger *RMSE*, which is consistent with the results of Sun et al. [24]. This phenomenon occurs because the seasonal variation at high latitudes is more substantial than that at low latitudes, which increases the difficulty of T_m modeling and eventually leads to larger *RMSEs* at high latitudes. At the same time, it can be seen in the figure that the *RMSEs* of the UNB3m model exhibit apparent differences in different latitude ranges. In contrast, the three hybrid models are uniformly distributed and stable. The *RMSEs* of the Bevis, GPT3, and HGPT models are much larger than those of the three hybrid models. Therefore, the method proposed in this study improves the accuracy of the model. Further, it makes the model accuracy more evenly distributed in space, owing to the introduction of geographic information into the model input layer.

Figure 9 shows that the *RMSEs* of the three hybrid models are much smaller than the UNB3m model. Simultaneously, compared with the *RMSEs* of the Bevis model, the GPT3 model, and the HGPT model, the hybrid models also have a significant improvement. The number of sites with an *RMSE* value smaller than 3.0 K is 0 for the UNB3m model, 74 for the hybrid model 1, 101 for the hybrid model 2, 89 for the hybrid model 3, 22 for the Bevis model, 20 for the GPT3 model, and 21 for the HGPT model. The above results show that the method proposed in this study significantly improves the model's accuracy, and hm2 performs best in all models.

Because latitude is an essential factor affecting T_m [6], we divided the study area into eight latitude bands with intervals of 5° to compare and analyze the performance of each model in different latitude bands. The results are shown in Figure 10.

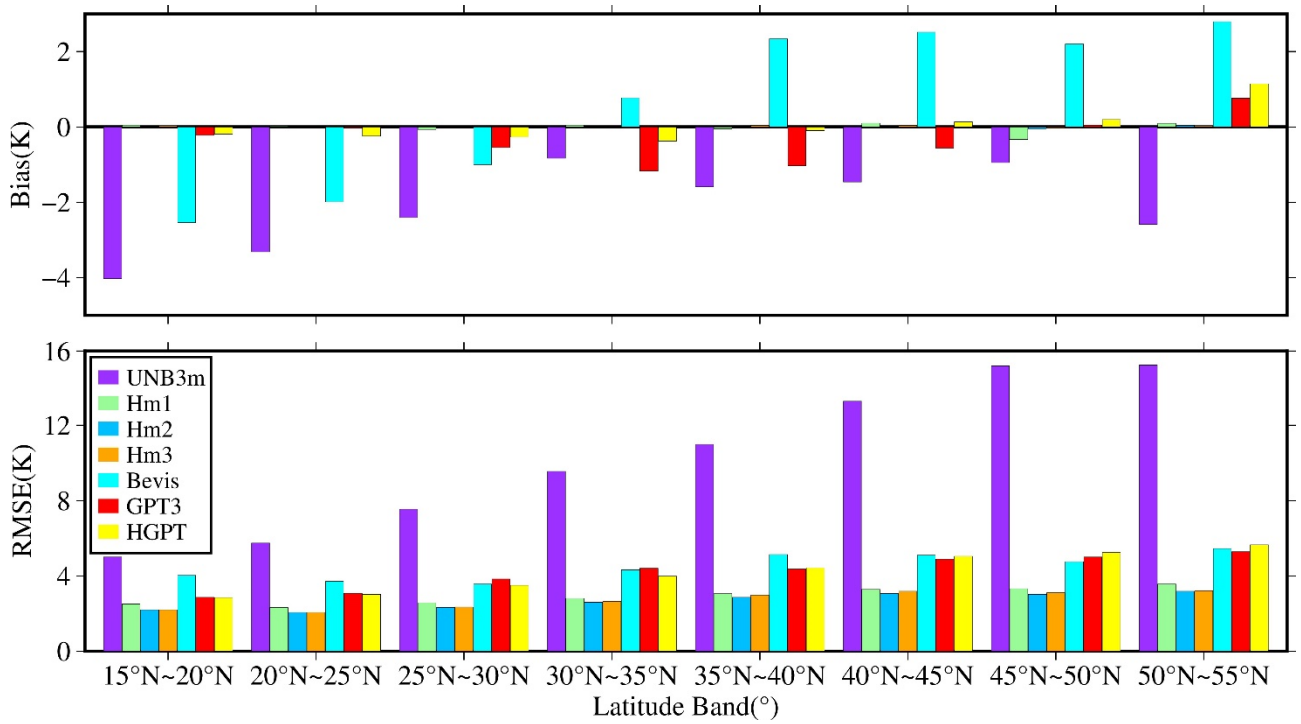

Figure 10. *Biases* and *RMSEs* of each model at different latitudes.

The *biases* of the three hybrid models at different latitudes are all close to zero, which indicates that the artificial neural network method has a noticeable effect on correcting the systematic error of the UNB3m model (Figure 10). The stability of the hybrid models at different latitudes is better than that of the Bevis, GPT3, and HGPT models (Figure 10). The *RMSEs* of all models are generally smaller at low latitudes and larger at high latitudes and show an increasing trend with increasing latitude, which is consistent with the results presented in Figure 8. Regardless of the latitude band, the *RMSEs* of the hybrid models were much lower than those of the Bevis, GPT3, and HGPT models, indicating that the three hybrid models significantly improved the accuracy of T_m. Furthermore, compared with the Bevis, GPT3, and HGPT models, the *RMSEs* of the three hybrid models are all within 2 to 3.6 K in different latitude bands, and the variation between various bands is slight and uniform, showing more notable advantages. Comparing the three hybrid models, the *RMSEs* of hm2 at different latitudes are slightly lower than those of the other two models. This result means that hm2 outperforms other models.

T_m is greatly affected by station altitude, and altitude differences may lead to uncertainties of T_m model accuracy [6]. Therefore, we divided the height into eight layers with an interval of 0.5 km and calculated *RMSEs* for each height layer. The results of the analysis are presented in Figure 11.

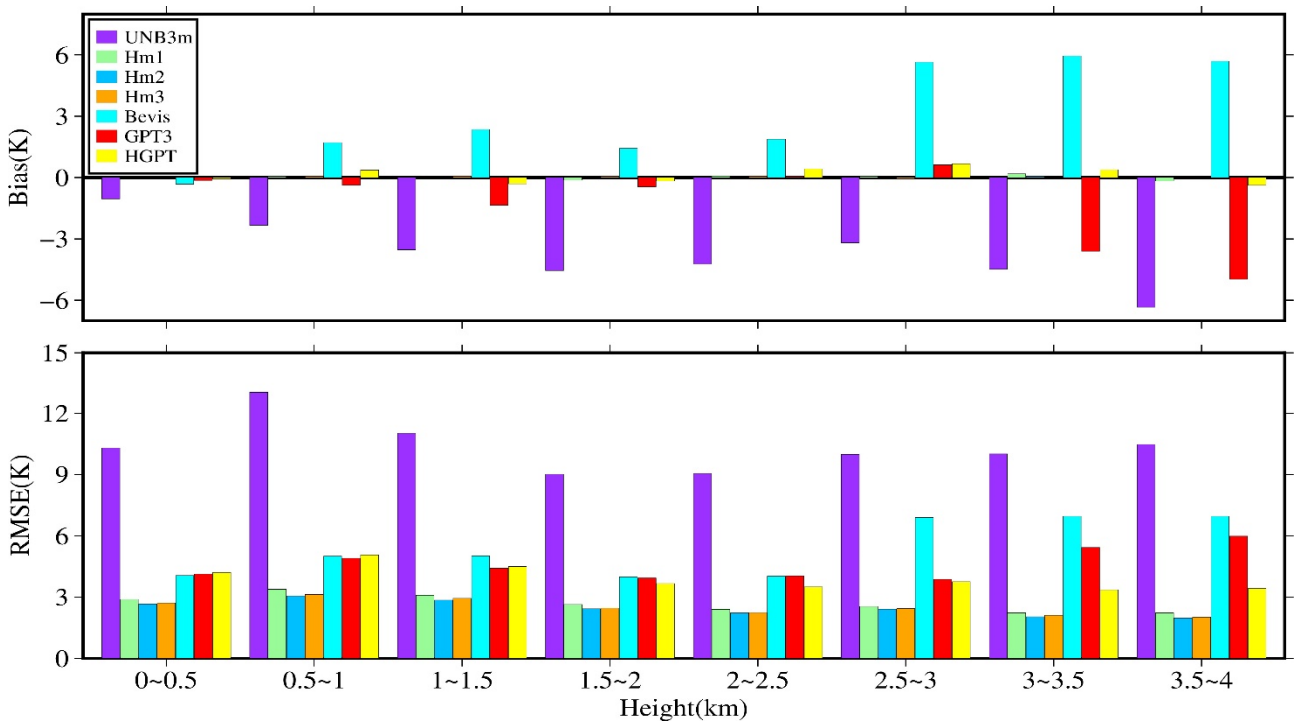

Figure 11. *Biases* and *RMSEs* of each model at different heights.

Figure 11 shows that the *biases* of the three hybrid models tend to be stable and remain near 0, indicating that the accuracies of the hybrid models at different heights are much better than the UNB3m model, Bevis model, GPT3 model, and HGPT model. The *RMSEs* of the hybrid models obtained after optimization by the artificial neural network methods are 30% lower, relative to the UNB3m model. The *RMSEs* of the three hybrid models decrease with the increase in altitude and are lower than that of the Bevis, GPT3, and HGPT models. Furthermore, most of the *RMSEs* of the three hybrid models were below 3 K and were much smaller than those of the UNB3m, Bevis, GPT3, and HGPT models. This result shows that the accuracies of the hybrid models are higher than those of the Bevis, GPT3, and HGPT models and have a more stable accuracy in the vertical direction.

Because T_m has prominent seasonal characteristics [6], we calculated the *biases* and *RMSEs* for the four seasons to analyze the temporal variation of the performance of each model, as shown in Figure 12.

Figure 12 shows that the UNB3m model shows poor accuracy in all seasons, especially in summer. However, after the correction by the artificial neural network methods, the accuracy in each season has been greatly improved. The *RMSE* in spring, autumn, and winter dropped to more than 50% of the UNB3m model, and the *RMSE* in summer directly decreased to more than 80%. In addition, the *RMSEs* of the hybrid models in each period are smaller than that of the Bevis, GPT3, and HGPT models, indicating the superiority of the hybrid model. The hybrid models have higher and more uniform accuracy in time. When comparing the three hybrid models, we can see that the *RMSEs* of hm2 are smaller than those of hm1 and hm3. Therefore, hm2 performs best in each season.

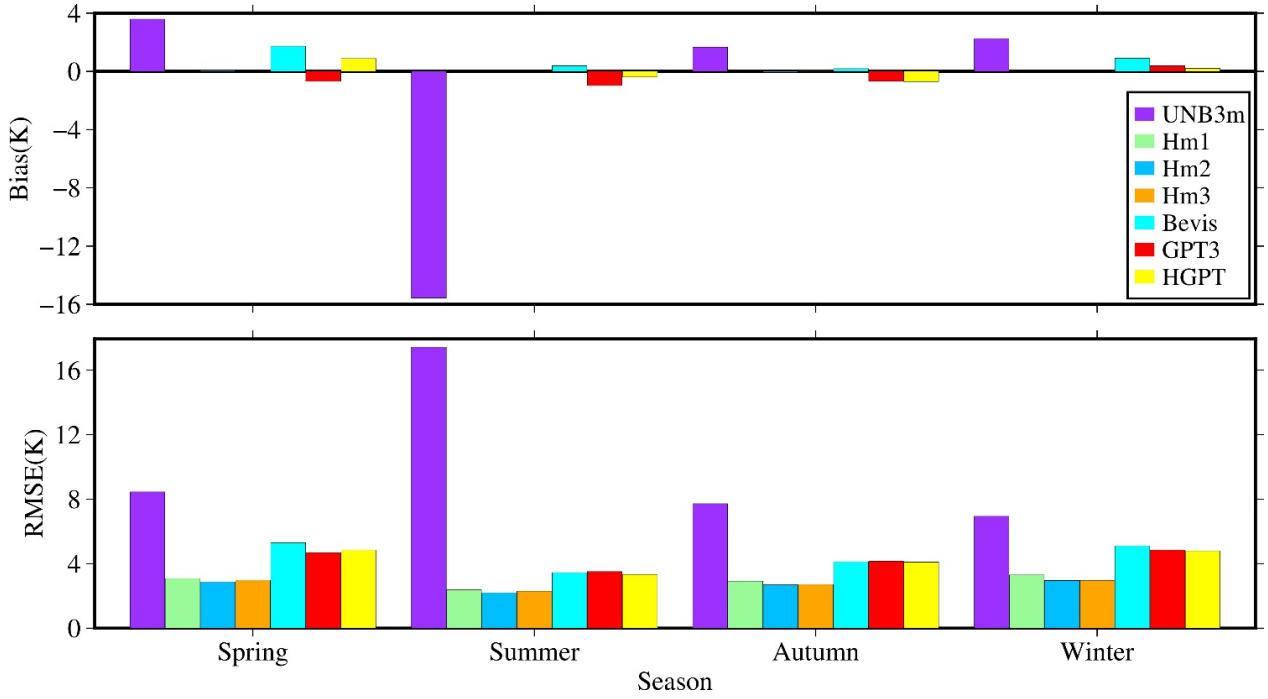

Figure 12. *Biases* and *RMSEs* of each model in different seasons.

4.3. Occupancy of Hybrid Models

We also compared the computer storage space and the number of parameters for each model, and the results are presented in Table 4.

Table 4. The computer storage space and the number of parameters for each model.

Model	Computer Storage Space	Number of Parameters
UNB3m	104 KB	103
Hm1	104 KB	104
Hm2	104 KB	104
Hm3	104 KB	104
GPT3	29,081.6 KB	324,003

Table 4 indicates that the computer storage space occupied by the three hybrid models is small and is reduced by 99.6% compared to that occupied by the GPT3 model. Compared with GPT3 model, the number of parameters was reduced by 99.2%. Therefore, the new model has a tremendous advantage in storage.

5. Applications of Hybrid Models in Retrieving PWV

From the performance discussions of the three hybrid models, we recommend hybrid model 2 (Hm2). The formula for calculating PWV by combining ZWD and T_m is as follows:

$$PWV = \Pi \times ZWD \tag{21}$$

$$\Pi = \frac{10^6}{\rho_w R_v \left[k_3 / T_m + k_2'\right]} \tag{22}$$

where ρ_w is the density of water and R_v is the specific gas constant.

To evaluate the effect of error in T_m on its synthesized PWV, a commonly used quantity is the relative error in $PWVs$ calculated using the following formula:

$$\frac{\sigma_{pwv}}{PWV} = \frac{\Pi(T_m + \sigma_{T_m}) - \Pi(T_m)}{\Pi(T_m)} = \frac{1 + \frac{k_2'}{k_3} T_m}{1 + \frac{k_2'}{k_3}(T_m + \sigma_{T_m})} \cdot \frac{T_m + \sigma_{T_m}}{Tm} - 1 \tag{23}$$

where σ_{pwv} is the error in PWV caused by the error in T_m and σ_{T_m}.

Since $k_2'/k_3 \approx 5.9 \times 10^{-5}$ K^{-1} and T_m is in the range from 220 K to 310 K in our experiment, Equation (23) can be simplified to [22,44]

$$\frac{\sigma_{pwv}}{PWV} \approx \frac{T_m + \sigma_{T_m}}{Tm} - 1 = \frac{\sigma_{T_m}}{Tm} \tag{24}$$

Assuming that there is no error in the value of ZWD, if the error of T_m is small, this will improve the converting accuracy of ZWD to PWV. Therefore, our established hybrid model will indirectly enhance the accuracy of PWV.

To further illustrate the improved accuracy of the hybrid model for PWV inversion, we selected four stations for analysis, and the station information is shown in Table 5. The $PWVs$ calculated from the ZWD and the T_m provided by the four radiosonde stations in 2016 were employed as a reference to validate the PWV mapped from radiosonde ZWD using the hybrid model 2/Bevis/GPT3/HGPT model. The results are shown in Figure 13, Tables 6 and 7.

Table 5. The information of the four stations.

Station Number	Latitude/°	Longitude/°	Altitude/m
58,457	30.23	120.16	43.1
50,557	49.16	125.23	242.6
51,463	43.78	89.61	921.4
45,004	22.33	114.17	66.17

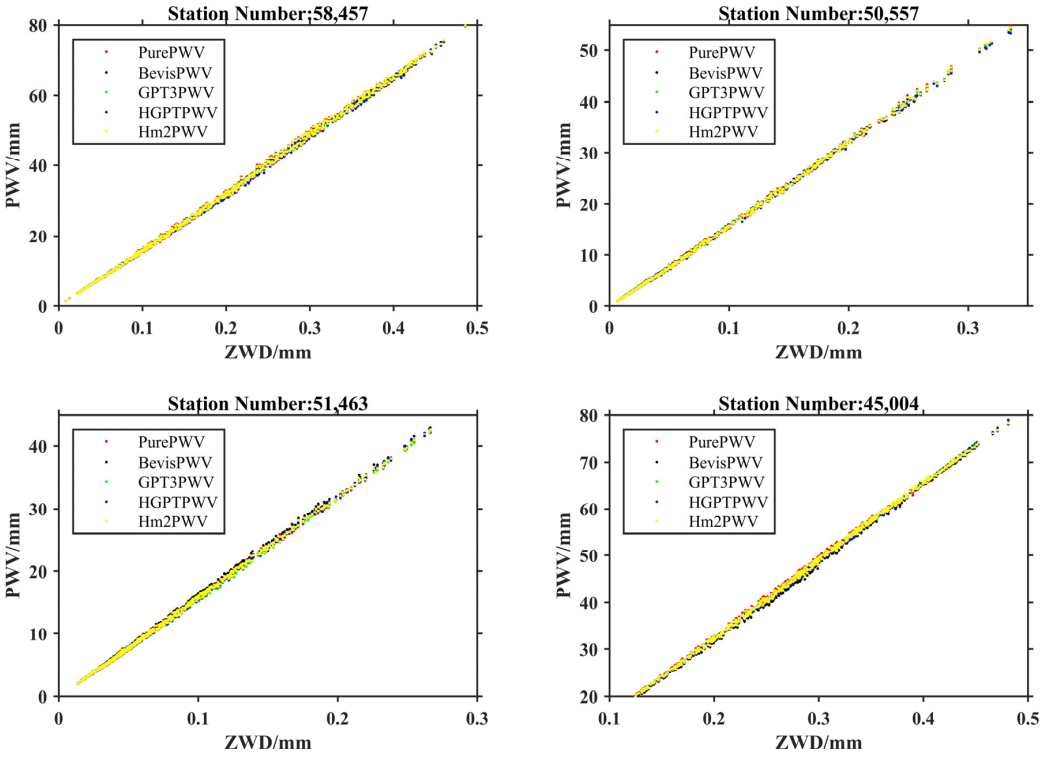

Figure 13. The PWV converted by the Bevis, GPT3, HGPT, and Hm2 models at four radiosonde stations.

Table 6. The *MAE* of the differences between the computed and the reference PWV.

Station Number	Hm1	Bevis	Change in	GPT3	Change in	HGPT	Change in
	MAE/mm	*MAE*/mm	%	*MAE*/mm	%	*MAE*/mm	%
58,457	0.150	0.224	49.3	0.332	121.2	0.332	121.2
50,557	0.067	0.134	99.8	0.137	104.2	0.157	133.5
51,463	0.080	0.169	112.0	0.166	108.2	0.154	92.5
45,004	0.169	0.381	124.7	0.307	81.3	0.308	82.0

Table 7. The *RMSE* of the differences between the computed and the reference PWV.

Station Number	Hm2	Bevis	Change in	GPT3	Change in	HGPT	Change in
	RMSE/mm	*RMSE*/mm	%	*RMSE*/mm	%	*RMSE*/mm	%
58,457	0.199	0.293	46.9	0.430	115.4	0.428	114.4
50,557	0.101	0.182	80.6	0.204	102.5	0.240	137.8
51,463	0.111	0.248	124.5	0.217	96.5	0.206	86.1
45,004	0.219	0.454	107.1	0.380	73.3	0.379	72.6

As shown in Figure 13, the PWV calculated by the hybrid model agrees better with the reference value, which shows that the hybrid model outperforms the Bevis, GPT3, and HGPT models in retrieving the PWV. The *RMSEs* of PWV derived from the Hm2 model are all less than 1 mm; the accuracy is very appreciable in weather research because the required RMS is 3 mm [45]. Tables 6 and 7 show that compared with the Bevis model, the retrieving PWV accuracy of the hybrid model is greatly improved, and its *MAE* is 96.5% lower on average than the Bevis model. The *RMSE* is 89.8% lower on average. The accuracy of the hybrid model in retrieving PWV has been dramatically improved in comparison with the GPT3 model and the HGPT model. Simultaneously, the *MAE* of the hybrid model decreased by 103.7% and 107.3% on average, and *RMSE* decreased by 96.9% and 102.7%, respectively. These proved that the hybrid model is superior to the Bevis, GPT3, and HGPT models in retrieving PWV.

To demonstrate the outperformance of the Hm2 for retrieving PWV more intuitively, Figure 14 gives *RMSEs* reduction at all radiosonde stations. Figure 14 illustrates that the Hm2 model shows smaller *RMSE* than other models at most stations. The mean *RMSE* reduction of the Hm2 model reaches up to 33.9% in comparison with Bevis, 36.4% in comparison with GPT3, and 37.0% in comparison with HGPT. It is interesting to note that the *RMSE* of the Hm2 PWV is reduced at all stations in China Mainland. Overall, the Hm2 model performs the best in mapping ZWD onto PWV.

To further verify the Hm2 has a significant improvement in accuracy compared to the comparison model, the *RMSE* of each model at each site was used as a sample for hypothesis testing. Set the null hypothesis H0: there is no significant difference between the *RMSE* of the comparison model at each site (sample X1) and the *RMSE* of the Hm2 model at each site (sample X2). Alternative hypothesis H1: there is a significant difference between X1 and X2. Due to the large sample size, the z-test [46] was used. Set the left-side confidence level to a = 0.05. Calculating the statistic z and looking up the table to get the corresponding *p* value, the result is shown in Table 8. By comparing the statistic z and the *p* value (p ($|Z| > 1.64$) = 0.05), we can see that the absolute value of the z of the three pairs of samples is larger than 1.64 in all cases, with the corresponding *p* less than 0.05. Therefore, the null hypothesis is finally rejected, indicating significant differences among the Hm2 *RMSEs* and other model's *RMSEs*. This result suggests that the Hm2 *RMSE* is improved significantly compared to that of other models at the 95% confidence level.

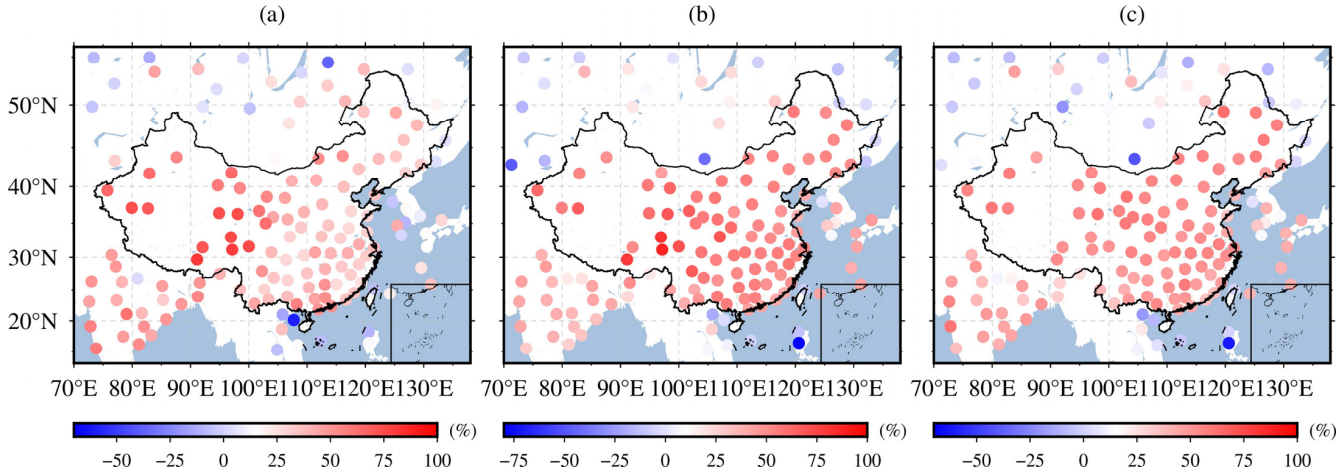

Figure 14. The *RMSE* reductions of the Hm2 model compared with different models for retrieving PWV: (**a**) Bevis model; (**b**) GPT3 model; (**c**) HGPT model.

Table 8. The statistic z and corresponding *p* value.

z (P)	Bevis	GPT3	HGPT
Hm2	−2.2463 (0.0122)	−2.7058 (0.003)	−2.6693 (0.004)

6. Conclusions

To overcome the drawbacks of existing T_m models with poor universality, profound local accuracy loss, and difficulty in reflecting the nonlinear relationship between T_m and meteorological parameters, this study used artificial neural network methods for constructing T_m hybrid models in China. Validated with radiosonde T_m, the accuracies of the three hybrid models were 2.954 K, 2.703 K, and 2.763 K in terms of *RMSE*. In view of *RMSE*, compared with the UNB3m model, the accuracies were improved by 73.1%, 75.3%, and 74.8%; for the Bevis model, accuracies were optimized by 35.3%, 40.8%, and 39.5%; and for the GPT3 model, accuracies were improved by 32.0%, 37.8%, and 36.4%, respectively. Moreover, the hybrid models effectively weakened the spatiotemporal variation in the accuracy of the UNB3m model and achieved higher and more uniform accuracy in space and time. Among the three hybrid models, hm2 exhibited the best performance, followed by hm3. The models constructed in this study had better accuracy than the three international models. Moreover, the computer storage space occupied by the new models is significantly lower than that of the GPT3 model, and the number of parameters is substantially reduced. The accuracy improvement in the best hybrid model's T_m on its resultant PWV at four exemplary radiosonde stations and the whole study area were investigated using the PWVs through the radiosonde ZWD and T_m. The *RMSEs* of PWV derived from the Hm2 model are all less than 1 mm at exemplary radiosonde stations; the accuracy meets the needs of weather research. The overall error of the best hybrid model's T_m in the resultant PWV is smaller than that of Bevis, GPT3, and HGPT models by 33.9%, 36.4%, and 37.0% in terms of *RMSE*. The results of hypothesis testing further proved that this accuracy improvement of the best hybrid T_m relative to the compared models is significant. The new models can be widely used to calculate high-precision T_m and are more suitable for GNSS receivers without large storage space.

However, the study area was mainly conducted in China, and the global regions need to be further examined to validate the new models. In addition, meteorological parameters (surface temperature and water vapor pressure) were considered when constructing the model in this study. In future research, we hope to develop a globally hybrid model that can calculate the T_m only based on geographical information (latitude, longitude, height) and temporal information (year, day of year (doy), hour of day (hod)).

Author Contributions: Data curation, L.L., L.H. (Liangke Huang), L.Z. and H.H.; formal analysis, M.C. and J.L.; investigation, J.L.; methodology, M.C. and J.L.; software, M.C. and J.L.; validation, M.C., J.L. and L.L.; writing—original draft preparation, J.L.; writing—review and editing, J.L., M.C., L.H. (Liangke Huang), L.Z. and L.H. (Ling Huang). All authors have read and agreed to the published version of the manuscript.

Funding: This work was supported by the Guangxi Natural Science Foundation of China (2020GXNSFBA297145), Foundation of Guilin University of Technology (GUTQDJJ6616032), National Natural Science Foundation of China (42074035, 41874033, 42064002), China Postdoctoral Science Foundation (2019T120687, 2018M630880), the Fundamental Research Funds for the Central Universities (2042020kf0009), Guangxi Science and Technology Base and Talent Project (No.AD1924 5060), and Innovation Project of Guangxi Graduate Education (YCSW2022 322).

Data Availability Statement: The radiosonde data can be accessed at http://www1.ncdc.noaa.gov/pub/data/igra/ (accessed on 16 January 2022). The UNB3m codes can be accessed at https://www2.unb.ca/gge/Resources/unb3m/unb3m.html (accessed on 16 January 2022). The GPT3 codes can be accessed at https://vmf.geo.tuwien.ac.at/codes/ (accessed on 16 January 2022). The HGPT codes can be accessed at https://github.com/pjmateus/hgpt_model (accessed on 18 July 2022). The training data and artificial neural network codes are available in https://github.com/jyli999/HmTm_models (accessed on 18 July 2022).

Acknowledgments: The authors would like to thank the University of New Brunswick (UNB) for providing the UNB3m codes, Vienna University of Technology for providing the GPT3 codes, and IGRA (Integrated Global Radiosonde Archive) for providing the radiosonde data. We would like to thank Mateus et al. for providing the HGPT codes.

Conflicts of Interest: The authors declare no conflict of interest.

References

1. Wang, J.H.; Zhang, L.Y. Climate applications of a global, 2-hourly atmospheric precipitable water dataset derived from IGS tropospheric products. *J. Geod.* **2009**, *83*, 209–217. [CrossRef]
2. Jin, S.; Luo, O.F. Variability and Climatology of PWV From Global 13-Year GPS Observations. *IEEE Trans. Geosci. Remote Sens.* **2009**, *47*, 1918–1924. [CrossRef]
3. Wang, J.; Balidakis, K.; Zus, F.; Chang, X.; Ge, M.; Heinkelmann, R.; Schuh, H. Improving the Vertical Modeling of Tropospheric Delay. *Geophys. Res. Lett.* **2022**, *49*, e2021GL096732. [CrossRef]
4. Wang, X.M.; Zhang, K.F.; Wu, S.Q.; He, C.Y.; Cheng, Y.Y.; Li, X.X. Determination of zenith hydrostatic delay and its impact on GNSS-derived integrated water vapor. *Atmos. Meas. Tech.* **2017**, *10*, 2807–2820. [CrossRef]
5. Li, W.; Yuan, Y.B.; Ou, J.K.; Chai, Y.J.; Li, Z.S.; Liou, Y.A.; Wang, N.B. New versions of the BDS/GNSS zenith tropospheric delay model IGGtrop. *J. Geod.* **2015**, *89*, 73–80. [CrossRef]
6. Bevis, M.; Businger, S.; Herring, T.A.; Rocken, C.; Anthes, R.A.; Ware, R.H. Gps Meteorology—Remote-Sensing of Atmospheric Water-Vapor Using the Global Positioning System. *J. Geophys. Res.-Atmos.* **1992**, *97*, 15787–15801. [CrossRef]
7. Yu, S.W.; Liu, Z.Z. Temporal and Spatial Impact of Precipitable Water Vapor on GPS Relative Positioning During the Tropical Cyclone Hato (2017) in Hong Kong and Taiwan. *Earth Space Sci.* **2021**, *8*, e2020EA001371. [CrossRef]
8. Zhao, Q.Z.; Liu, Y.; Ma, X.W.; Yao, W.Q.; Yao, Y.B.; Li, X. An Improved Rainfall Forecasting Model Based on GNSS Observations. *IEEE Trans. Geosci. Remote Sens.* **2020**, *58*, 4891–4900. [CrossRef]
9. Zhang, H.X.; Yuan, Y.B.; Li, W.; Ou, J.K.; Li, Y.; Zhang, B.C. GPS PPP-derived precipitable water vapor retrieval based on T-m/P-s from multiple sources of meteorological data sets in China. *J. Geophys. Res.-Atmos.* **2017**, *122*, 4165–4183. [CrossRef]
10. Wang, X.M.; Zhang, K.F.; Wu, S.Q.; Fan, S.J.; Cheng, Y.Y. Water vapor-weighted mean temperature and its impact on the determination of precipitable water vapor and its linear trend. *J. Geophys. Res.-Atmos.* **2016**, *121*, 833–852. [CrossRef]
11. Yao, Y.; Zhang, B.; Xu, C.; Yan, F. Improved one/multi-parameter models that consider seasonal and geographic variations for estimating weighted mean temperature in ground-based GPS meteorology. *J. Geod.* **2013**, *88*, 273–282. [CrossRef]
12. Jin, S.G.; Li, Z.; Cho, J. Integrated Water Vapor Field and Multiscale Variations over China from GPS Measurements. *J. Appl. Meteorol. Climatol.* **2008**, *47*, 3008–3015. [CrossRef]
13. Lee, S.W.; Kouba, J.; Schutz, B.; Kim, D.H.; Lee, Y.J. Monitoring precipitable water vapor in real-time using global navigation satellite systems. *J. Geod.* **2013**, *87*, 923–934. [CrossRef]
14. Emardson, T.R.; Elgered, G.; Johansson, J.M. Three months of continuous monitoring of atmospheric water vapor with a network of Global Positioning System receivers. *J. Geophys. Res.-Atmos.* **1998**, *103*, 1807–1820. [CrossRef]
15. Ross, R.J.; Rosenfeld, S. Estimating mean weighted temperature of the atmosphere for Global Positioning System applications. *J. Geophys. Res.-Atmos.* **1997**, *102*, 21719–21730. [CrossRef]
16. Wang, S.M.; Xu, T.H.; Nie, W.F.; Wang, J.; Xu, G.C. Establishment of atmospheric weighted mean temperature model in the polar regions. *Adv. Space Res.* **2020**, *65*, 518–528. [CrossRef]

17. Liu, C.; Zheng, N.S.; Zhang, K.F.; Liu, J.Y. A New Method for Refining the GNSS-Derived Precipitable Water Vapor Map. *Sensors* **2019**, *19*, 698. [CrossRef] [PubMed]
18. Liu, J.H.; Yao, Y.B.; Sang, J.Z. A new weighted mean temperature model in China. *Adv. Space Res.* **2018**, *61*, 402–412. [CrossRef]
19. Bohm, J.; Moller, G.; Schindelegger, M.; Pain, G.; Weber, R. Development of an improved empirical model for slant delays in the troposphere (GPT2w). *GPS Solut.* **2015**, *19*, 433–441. [CrossRef]
20. Schuler, T. The TropGrid2 standard tropospheric correction model. *GPS Solut.* **2014**, *18*, 123–131. [CrossRef]
21. Leandro, R.F.; Langley, R.B.; Santos, M.C. UNB3m_pack: A neutral atmosphere delay package for radiometric space techniques. *GPS Solut.* **2008**, *12*, 65–70. [CrossRef]
22. Yao, Y.B.; Xu, C.Q.; Zhang, B.; Cao, N. GTm-III: A new global empirical model for mapping zenith wet delays onto precipitable water vapour. *Geophys. J. Int.* **2014**, *197*, 202–212. [CrossRef]
23. Landskron, D.; Bohm, J. VMF3/GPT3: Refined discrete and empirical troposphere mapping functions. *J. Geod.* **2018**, *92*, 349–360. [CrossRef] [PubMed]
24. Sun, Z.Y.; Zhang, B.; Yao, Y.B. An ERA5-Based Model for Estimating Tropospheric Delay and Weighted Mean Temperature Over China With Improved Spatiotemporal Resolutions. *Earth Space Sci.* **2019**, *6*, 1926–1941. [CrossRef]
25. Mateus, P.; Catalão, J.; Mendes, V.B.; Nico, G. An ERA5-Based Hourly Global Pressure and Temperature (HGPT) Model. *Remote Sens.* **2020**, *12*, 1098. [CrossRef]
26. Mateus, P.; Mendes, V.B.; Plecha, S.M. HGPT2: An ERA5-Based Global Model to Estimate Relative Humidity. *Remote Sens.* **2021**, *13*, 2179. [CrossRef]
27. Huang, L.K.; Liu, L.L.; Chen, H.; Jiang, W.P. An improved atmospheric weighted mean temperature model and its impact on GNSS precipitable water vapor estimates for China. *GPS Solut.* **2019**, *23*, 51. [CrossRef]
28. Yuan, Q.Q.; Xu, H.Z.; Li, T.W.; Shen, H.F.; Zhang, L.P. Estimating surface soil moisture from satellite observations using a generalized regression neural network trained on sparse ground-based measurements in the continental U.S. *J. Hydrol.* **2020**, *580*, 124351. [CrossRef]
29. Shamshiri, R.; Motagh, M.; Nahavandchi, H.; Haghighi, M.H.; Hoseini, M. Improving tropospheric corrections on large-scale Sentinel-1 interferograms using a machine learning approach for integration with GNSS-derived zenith total delay (ZTD). *Remote Sens. Environ.* **2020**, *239*, 111608. [CrossRef]
30. Li, L.; Xu, Y.; Yan, L.Z.; Wang, S.L.; Liu, G.L.; Liu, F. A Regional NWP Tropospheric Delay Inversion Method Based on a General Regression Neural Network Model. *Sensors* **2020**, *20*, 3167. [CrossRef]
31. Ding, M.H. A neural network model for predicting weighted mean temperature. *J. Geod.* **2018**, *92*, 1187–1198. [CrossRef]
32. Klos, A.; Hunegnaw, A.; Teferle, F.N.; Abraha, K.E.; Ahmed, F.; Bogusz, J. Statistical significance of trends in Zenith Wet Delay from re-processed GPS solutions. *GPS Solut.* **2018**, *22*, 51. [CrossRef]
33. Mao, J.; Wang, Q.; Liang, Y.; Cui, T. A new simplified zenith tropospheric delay model for real-time GNSS applications. *GPS Solut.* **2021**, *25*, 43. [CrossRef]
34. Rumelhart, D.E.; Hinton, G.E.; Williams, R.J. Learning representations by back-propagating errors. *Nature* **1986**, *323*, 533–536. [CrossRef]
35. Hecht-Nielsen, R. Theory of the backpropagation neural network. In *Neural Networks for Perception*; Academic Press: Cambridge, UK, 1992; pp. 65–93.
36. Hornik, K.; Stinchcombe, M.; White, H. Multilayer feedforward networks are universal approximators. *Neural Netw.* **1989**, *2*, 359–366. [CrossRef]
37. Yao, Y.B.; Sun, Z.Y.; Xu, C.Q. Establishment and Evaluation of a New Meteorological Observation-Based Grid Model for Estimating Zenith Wet Delay in Ground-Based Global Navigation Satellite System (GNSS). *Remote Sens.* **2018**, *10*, 1718. [CrossRef]
38. Breiman, L. Random Forests. *Mach. Learn.* **2001**, *45*, 5–32. [CrossRef]
39. Specht, D.F. A general regression neural network. *IEEE Trans Neural Netw* **1991**, *2*, 568–576. [CrossRef]
40. Rodriguez, J.D.; Perez, A.; Lozano, J.A. Sensitivity Analysis of k-Fold Cross Validation in Prediction Error Estimation. *IEEE Trans. Pattern Anal. Mach. Intell.* **2010**, *32*, 569–575. [CrossRef]
41. Sun, Z.; Zhang, B.; Yao, Y. Improving the Estimation of Weighted Mean Temperature in China Using Machine Learning Methods. *Remote Sens.* **2021**, *13*, 1016. [CrossRef]
42. Reich, S.L.; Gomez, D.R.; Dawidowski, L.E. Artificial neural network for the identification of unknown air pollution sources. *Atmos. Environ.* **1999**, *33*, 3045–3052. [CrossRef]
43. Gardner, M.W.; Dorling, S.R. Artificial neural networks (the multilayer perceptron)—A review of applications in the atmospheric sciences. *Atmos. Environ.* **1998**, *32*, 2627–2636. [CrossRef]
44. Wang, J.H.; Zhang, L.Y.; Dai, A. Global estimates of water-vapor-weighted mean temperature of the atmosphere for GPS applications. *J. Geophys. Res.-Atmos.* **2005**, *110*, D21101. [CrossRef]
45. Yuan, Y.; Zhang, K.; Rohm, W.; Choy, S.; Norman, R.; Wang, C.-S. Real-time retrieval of precipitable water vapor from GPS precise point positioning. *J. Geophys. Res.-Atmos.* **2014**, *119*, 10044–10057. [CrossRef]
46. Chen, M. F-test and z-test for high-dimensional regression models with a factor structure. *J. Stat. Comput. Simul.* **2022**, 1–20. [CrossRef]